Wang *et al. Microstructures* **2025**, *5*, 2025044
DOI: 10.20517/microstructures.2024.130

Microstructures

Research Article

Open Access

Shape memory of bcc structured high-entropy-alloy nanowires during room temperature deformation

Zhanxin Wang[1], Shuai Li[1], Huibin Lian[1], Yufeng Zhao[1], Zhipeng Li[1], Yadi Zhai[2], Haibo Long[2], Lihua Wang[2], Xiaodong Han[2]

[1]School of Physics and Optoelectronic Engineering, Beijing University of Technology, Beijing 100124, China.
[2]Faculty of Materials and Manufacturing, Beijing University of Technology, Beijing 100124, China.

Correspondence to: Prof. Yadi Zhai, Faculty of Materials and Manufacturing, Beijing University of Technology, No. 100 Pingleyuan, Chaoyang District, Beijing 100124, China. E-mail: ydzhai@bjut.edu.cn; Prof. Haibo Long, Faculty of Materials and Manufacturing, Beijing University of Technology, No. 100 Pingleyuan, Chaoyang District, Beijing 100124, China. E-mail: hblong@bjut.edu.cn; Prof. Lihua Wang, Faculty of Materials and Manufacturing, Beijing University of Technology, No. 100 Pingleyuan, Chaoyang District, Beijing 100124, China. E-mail: wlh@bjut.edu.cn

How to cite this article: Wang, Z.; Li, S.; Lian, H.; Zhao, Y.; Li, Z.; Zhai, Y.; Long, H.; Wang, L.; Han, X. Shape memory of bcc structured high-entropy-alloy nanowires during room temperature deformation. *Microstructures* **2025**, *5*, 2025044. https://dx.doi.org/10.20517/microstructures.2024.130

Received: 19 Nov 2024 **First Decision:** 13 Jan 2025 **Revised:** 10 Feb 2025 **Accepted:** 20 Feb 2025 **Published:** 17 Apr 2025

Academic Editor: Huijun Li **Copy Editor:** Fangling Lan **Production Editor:** Fangling Lan

Abstract

The deformation mechanism of body-centered cubic (bcc) structured high-entropy alloys (HEAs) has been the subject of considerable research interest. Although a considerable number of studies have been conducted, the majority have focused on relatively large HEAs. As the size of bcc structured HEAs decreases to the nanometer scale, the manner in which they accommodate plastic deformation remains unclear. In this study, we employed molecular dynamics simulations to investigate the mechanical behavior of HfNbTaTiZr HEA nanowires during tensile loading and unloading. The results demonstrated that the plastic deformation of HEA nanowires was governed by a transition from the bcc phase to the hexagonal close-packed (hcp) phase. This contrasts with previous studies that attributed the deformation to screw dislocation activities. The bcc-hcp phase transition was found to occur via Bain strain, which involves lattice distortion and atomic rearrangement, ultimately resulting in the formation of the hcp phase. Notably, this bcc-hcp phase transition was reversible upon unloading, demonstrating a shape memory effect. This phase transition and its recoverable nature at room temperature were rarely reported in bcc structured HEAs. Our findings provide a comprehensive understanding of the deformation mechanisms of nano-sized HEAs.

Keywords: High-entropy-alloy, phase transition, molecular dynamics simulation, nanowires, reversible

INTRODUCTION

High-entropy alloys (HEAs), a unique class of solid solutions characterized by equimolar or near-equimolar ratios of various elements, have attracted considerable attention for their remarkable mechanical properties[1-7]. Over the past few decades, numerous studies have been carried out to investigate the mechanical behaviors and deformation mechanisms of HEAs[8-16]. Specifically, previous studies have found that HEAs with a face-centered cubic (fcc) structure exhibit excellent plastic deformation capabilities, which are attributed to their multiple deformation mechanisms[9-12], including dislocation gliding, cross-slip, twinning, dislocation climbing, and phase transition from fcc to body-centered cubic (bcc). While for bcc structured HEAs, the majority of previous research has suggested that their deformation is primarily controlled by screw dislocation activities[13-20]. For instance, Couzinié *et al.* demonstrated that the plastic deformation of bcc structured HEAs is governed by non-uniform distributions of screw dislocations during the initial deformation stage[15]. Given that most dislocations in bcc structured HEAs are of the screw type and exhibit low mobility, these alloys typically display limited ductility[20-25]. However, Lee *et al.* revealed a notable exception, highlighting the role of edge dislocations in enhancing the strength of certain bcc structured HEAs[16]. Their findings indicated that edge dislocations in NbTaTiV HEAs can overcome high energy barriers and glide, thereby enabling the alloy to maintain its high strength. Generally, it is well-established that the deformation of bcc structured HEAs at room temperature is predominantly controlled by dislocation activities, while phase transitions tend to occur more readily at elevated temperatures[20]. Nevertheless, the majority of these studies have focused on large-scale HEAs, leaving a significant gap in understanding how bcc structured HEAs respond to deformation when their size is reduced to the nanoscale.

In nano-sized bcc structured elemental metals, such as tungsten (W) nanowires (NWs), it has been observed that plastic deformation is dominated by deformation twins[26]. Notably, these results also demonstrated that the deformation twins can revert to their original state after the removal of strain or stress. This finding challenges the widely accepted notion that plastic deformation typically causes irreversible structural changes in larger metals. The reversible deformation phenomena have typically only been reported in shape memory alloys[27,28] and have not been documented in bcc structured elemental metals or HEAs. As the material size approaches the nanoscale, predicting the behavior of bcc structured HEAs during deformation becomes increasingly complex. It remains unresolved whether phase transitions can occur in nano-sized bcc structured HEAs during deformation at room temperature, and whether such transitions are reversible upon removal of strain or stress.

This study investigates the mechanical behavior of HfNbTaTiZr HEA NWs during tensile loading and unloading at room temperature using molecular dynamics (MD) simulations. It was found that the plastic deformation of HfNbTaTiZr NWs was governed by a phase transition from bcc to hexagonal close-packed (hcp) during tensile loading. Two-dimensional (2D) and three-dimensional (3D) characterizations revealed that this bcc-hcp phase transition was achieved by Bain strain, which is a rare occurrence in bcc structured HEA NWs. It is noteworthy that this phase transition was reversible upon unloading, demonstrating a shape memory effect. This finding not only provides new insights into the deformation mechanisms of bcc structured HEAs at the nanoscale, but also opens up new avenues for their potential application in micro- and nano-devices.

MATERIALS AND METHODS

The simulations were conducted using the Large-Scale Atomic/Molecular Massively Parallel Simulator (LAMMPS)[29], with an embedded atom method (EAM) potential[30]. The potential used for current study can accurately describe the physical and mechanical properties of HfNbTaTiZr, including lattice constants,

elastic constants, cohesive energies and vacancy formation energies, and has proven effective in simulating the mechanical behavior of complex metallic systems[30]. In considering the diversity of local structures of HEAs, tens of random solid solution HfNbTaTiZr HEA NW models with different sizes and orientations have been constructed for simulations. It should be noted that solid solutions will not always be completely random or ideal; rather, they will exhibit short-range ordering (SRO)[31-34]. Thus, several models with different SRO degrees were constructed via hybrid Monte Carlo (MC)/MD simulations for comparative analysis. The Warren Cowley parameters (WCPs) for all elemental pairs were used to describe SRO[35,36]. The atom types are identified by Interval Common Neighbour Analysis (i-CNA)[37] using the Open Visualization Tool (OVITO)[38]. See more detailed methods in Supplementary Materials. Figure 1 depicts the initial structure of a typical random solid solution HfNbTaTiZr HEA NW. Figure 1A depicts the 3D model, wherein the Hf, Nb, Ta, Ti, and Zr atoms are represented in red, blue, yellow, purple, and green colors, respectively. The x, y, and z axes correspond to the $[1\bar{1}0]$, [001] and [110] directions, respectively. The dimensions of this HfNbTaTiZr HEAs NW are as follows: the length (x) is 47.9 nm, the width (y) is 5 nm, and the height (z) is 3.6 nm. Figure 1B depicts the 2D structure observed along the [001] direction. The model's surfaces were kept free, and the structure's energy was minimized through the application of the conjugate gradient method in order to achieve stability. Subsequently, the HfNbTaTiZr HEA NW was subjected to a relaxation process in an NVT ensemble for 500 ps at 300 K prior to loading. Finally, several layers of atoms at the extremities of the NW were fixed as rigid-body loading handles, and tensile loading and unloading were applied along the $[1\bar{1}0]$ direction.

RESULTS AND DISCUSSION

Figure 2 shows the atomic configuration evolution and the corresponding stress-strain curves of HfNbTaTiZr HEA NW under tensile loading and unloading conditions, where blue, red and green colors indicate the bcc, hcp and fcc structures, respectively. The strain rate remains at 1×10^8. As illustrated in Figure 2A-H, the deformation-induced bcc-hcp phase transition (atomic color changes from blue to red) exhibits reversible behavior, manifesting a pseudo-elastic phenomenon. Figure 2A depicts the pristine NW structure, which is clearly bcc. With loading, red atoms (hcp phase) begin to appear when the strain reaches 2.5% [Figure 2B], indicating the onset of the phase transition from bcc to hcp. Then, as the strain increases, more atoms transition from the bcc (blue) to the hcp (red) structure, with the hcp phase extending towards the ends of the NW [Figure 2C-E]. During the loading process depicted in Figure 2A-E, dislocation activity in the bcc regions is minimal, indicating that plastic deformation of this HfNbTaTiZr HEA NW is predominantly controlled by the bcc-hcp phase transition. Based on our simulations with different strain rates (5×10^7, 5×10^8, 1×10^9), as shown in Supplementary Figures 1-3, the results reveal that the bcc-hcp phase transition is the dominant plastic deformation behavior at different strain rates, indicating the onset of this phase transition is minimally affected by the strain rate. The difference is that the phase transition is initiated at multiple sites simultaneously and expands faster as the strain rate increases. Notably, this room-temperature phase transition is rarely reported and contrasts with prior studies suggesting that phase transitions typically occur under high-temperature conditions[17,23-25]. And interestingly, as shown in Figure 2F-H, the bcc-hcp phase transition is reversible upon unloading. Figure 2H shows that the hcp phase is almost entirely absent, leaving only the bcc atoms (blue). Figure 2I plots the stress-strain curve of this HfNbTaTiZr HEA NW during tensile loading and unloading. It can be observed that as the stress approaches ~ 2.7 GPa (the elastic strain is ~ 2.8%), the bcc-hcp phase transition is initiated. With the rapid expansion of the hcp phase, the stress first drops sharply and then rises slowly with slight fluctuations to 2.3 Gpa until the strain approaches 10%. The fluctuating increase in stress can be attributed to the fact that when the hcp phase reaches a sufficient size, some deformation occurs within the hcp phase, rather than merely phase boundary migration (see detailed analysis in Supplementary Figure 4). Generally, a stress of approximately 2.7 GPa is necessary to initiate the bcc-hcp phase transition, while approximately 2 GPa is

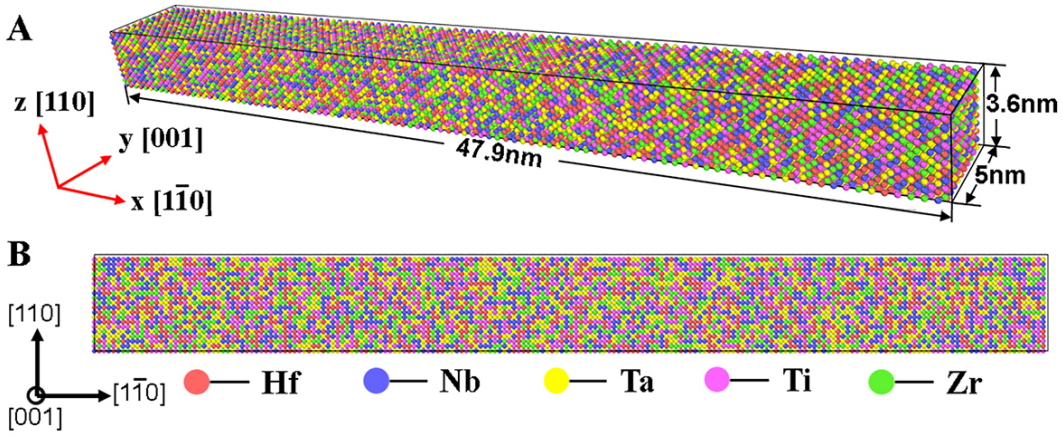

Figure 1. The initial atomic configuration of a typical random solid solution HfNbTaTiZr HEA NW. (A) depicts the 3D structure of the model, while (B) provides a 2D projection along the [001] direction. In the projection, different elemental atoms are represented by distinct colors: red for Hf, blue for Nb, yellow for Ta, pink for Ti, and green for Zr.

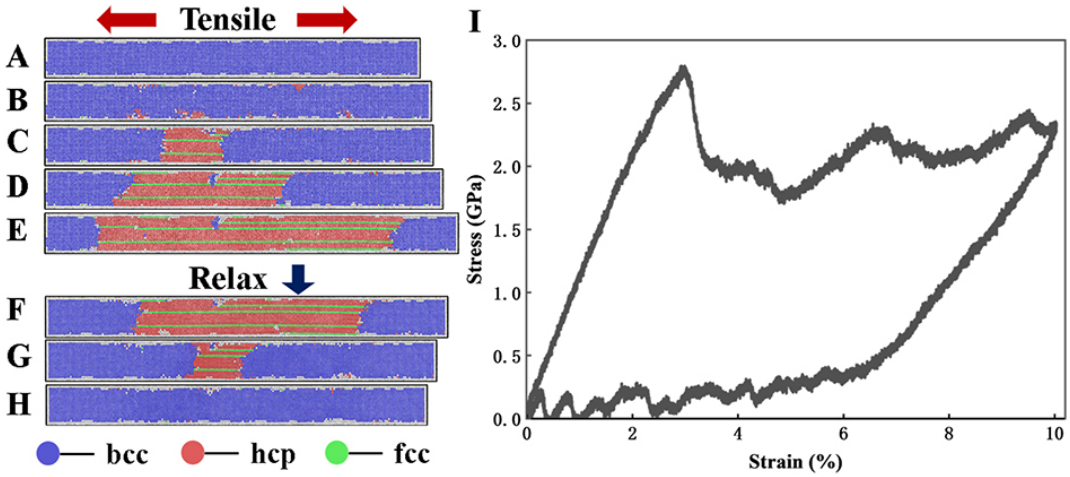

Figure 2. (A-H) Illustrates the atomic configuration evolution of the HfNbTaTiZr HEA NW during tension (A-E) and unloading (F-H) processes at 300 K. In these figures, blue signifies the bcc structure, red denotes the hcp structure, and green represents the fcc structure. (I) Presents the stress-strain curve corresponding to the processes shown in (A-H).

required for the subsequent growth of the hcp phase. Upon unloading, the stress-strain curve of the NW nearly recovers to its initial state, consistent with the observations in Figure 2F-H.

To clarify the bcc-hcp phase transition, Figure 3 presents enlarged images depicting the nucleation and growth of the hcp phase in HfNbTaTiZr HEA NW. Figure 3A-C illustrates the nucleation process of the hcp phase, while Figure 3D-F depicts its growth. As shown in Figure 3A and B, several red hcp-type atoms appear near the surface of the NW, and this hcp phase grows with continued straining. Comparing Figure 3B and C, it is observed that several white unknown atoms emerge before the propagation of the hcp phase. These white atoms are highly distorted bcc lattice atoms, suggesting that the phase transition from bcc to hcp follows the Bain straining path proposed by previous theoretical models[17]. Due to the different lattice parameters of the bcc and hcp phases, the interface between these phases in HfNbTaTiZr HEA NW experiences significant stress concentration, which further facilitates the bcc-hcp transition. Consequently, after the initiation of the hcp phase, it continues to grow within the NW, as shown in Figure 3D-F.

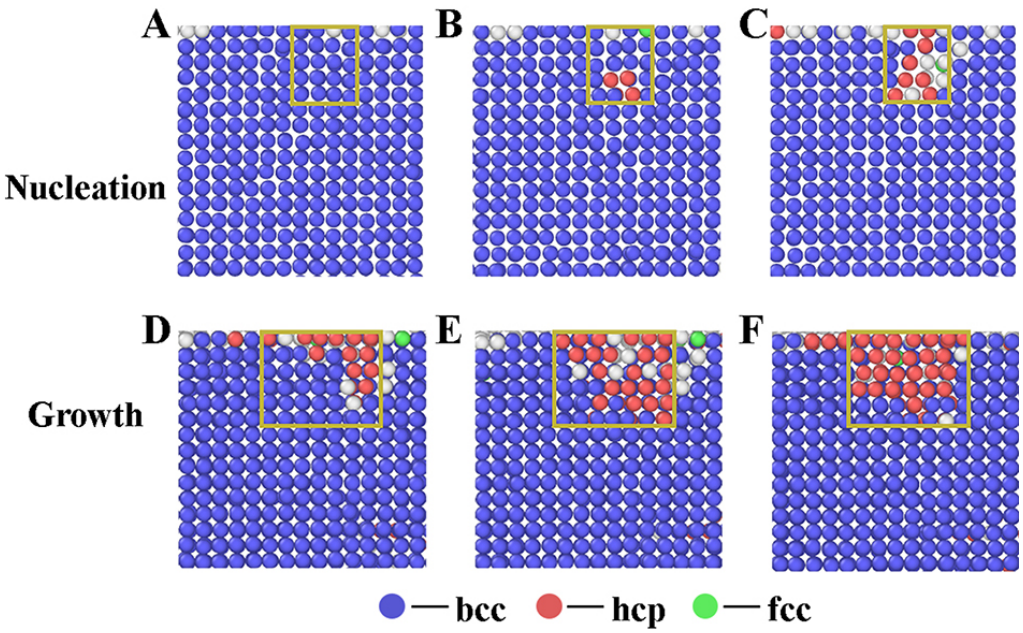

Figure 3. The atomic-scale deformation mechanisms of the HfNbTaTiZr HEA NW during the stretching process include the nucleation (A-C) and growth (D-F) of the hcp phase.

Figure 4 illustrates the 3D structural evolution during the bcc-hcp phase transition process. These figures facilitate a deeper comprehension of the phase transition mechanism in the HfNbTaTiZr HEA NW. Figure 4A presents a 3D image of the HfNbTaTiZr HEA NW prior to deformation. Figure 4B shows that several bcc lattices are significantly distorted when the applied stress exceeds the elastic limit (for a clearer view, see Figure 4G). As strain increases, as depicted in Figure 4C, many white atoms emerge and serve as nucleation sites for the hcp phase. This observation confirms that the bcc-hcp phase transition occurs via the Bain straining path[39]. With further straining, the hcp phase continues to grow and propagate throughout the NW, eventually converting almost all lattices to the hcp phase [Figure 4D and E]. Interestingly, as shown in Figure 4E, during the hcp phase propagation process, a fcc atomic layer is formed via Bain straining path[39]. During the loading process, these green atoms undergo only negligible shuffling, while atoms in their upper and lower atomic layers move to the left and right, respectively, leading to the formation of the fcc lattice (see more details in Supplementary Figure 5). To provide a clearer view of this phase transition, Figure 4F-J shows the enlarged images of the initial hcp nucleation region, illustrating how the bcc lattice distorts and ultimately transforms into the hcp phase. Comparing Figure 4F and G, the bcc lattices are noticeably distorted, as evidenced by changes in lattice spacing and bond angles. Continuous straining further increases these distortions, resulting in some atoms transforming into unknown atomic types (depicted in white), which no longer conform to the bcc structure [Figure 4H]. This distortion increases the crystal's internal energy and provides a driving force for the propagation of the hcp phase. As straining continues, these highly distorted atoms undergo a rearrangement process, and their interactions gradually adjust, ultimately forming the hcp lattice [Figure 4I and J].

Interestingly, our MD simulations reveal that the hcp phase can reverse to the bcc phase upon unloading. Figure 5 illustrates the structural evolution of the HfNbTaTiZr HEA NW during unloading, highlighting the transition from the hcp phase to the bcc phase during the reverse phase transition. Light blue frames in the figures denote the same region within the NW, allowing for clear tracking of the recovery process by comparing changes in atomic color within these frames. Figure 5A-C shows a representative example where

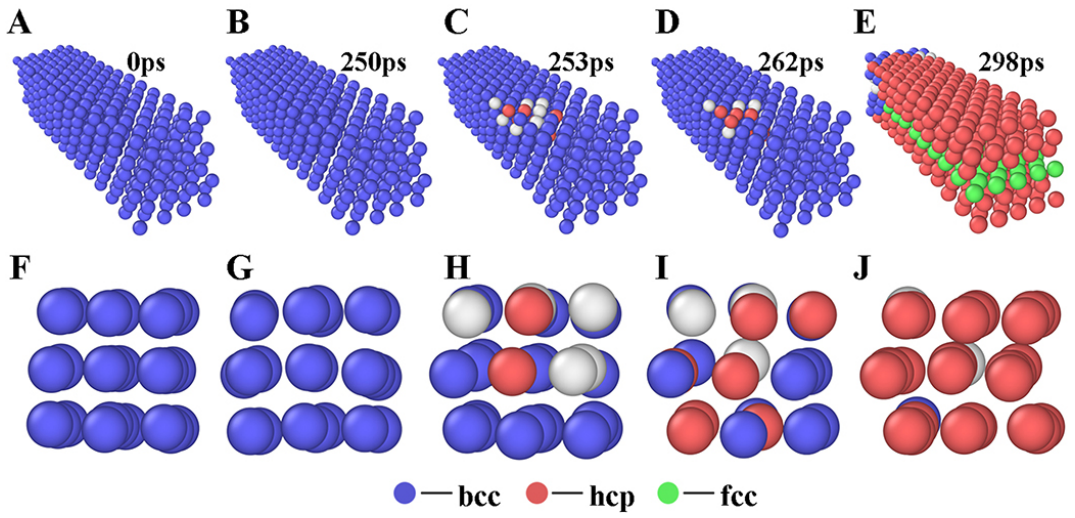

Figure 4. (A-E) Illustrates the 3D structural evolution of the HfNbTaTiZr HEA NW during the hcp nucleation process, within a strain range of 2.5% to 2.6%. (F-J) Provides enlarged images of the initial hcp nucleation region in the HfNbTaTiZr HEA NW.

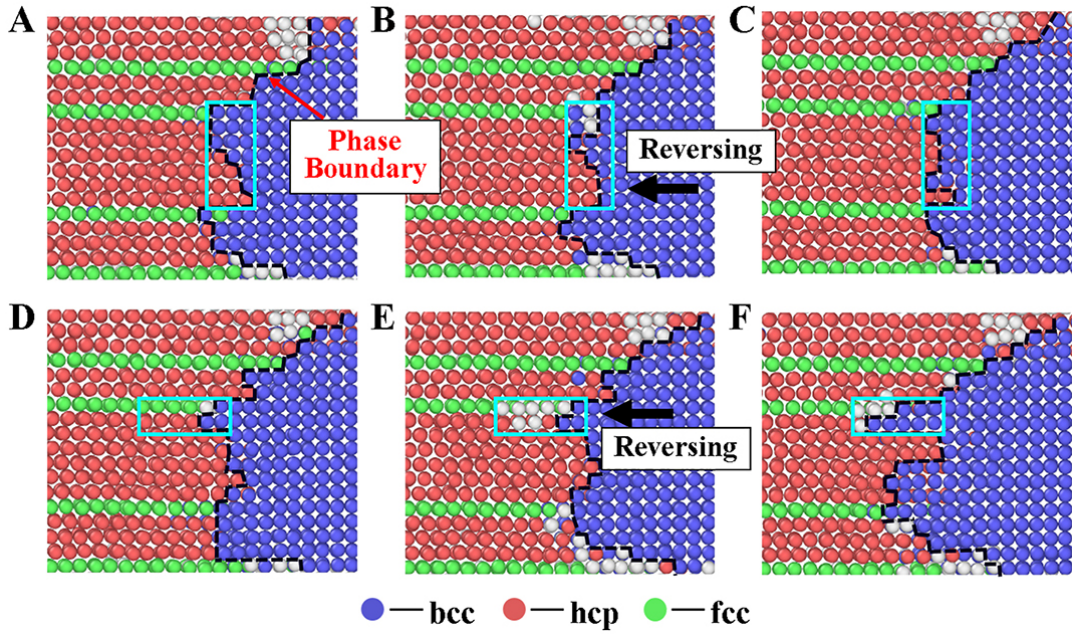

Figure 5. (A-F) Illustrates the atomic-scale mechanism of the reverse phase transition in the HfNbTaTiZr HEA NW during the unloading process.

hcp atoms at the phase boundary transform into bcc atoms. By comparing the atomic colors in the light blue framed regions of Figure 5A and B, several atoms near the phase boundary gradually change from their initial color to white, indicating lattice distortion. Continued unloading causes this distortion to propagate, with some neighboring red hcp atoms eventually transforming into blue bcc atoms [Figure 5C]. Figure 5D-F presents another instance of the hcp-bcc phase transition, providing a clearer view of the transition path. As shown by the light blue frames, many red hcp-type atoms near the phase boundary first turn white and then transition to blue bcc-type, paralleling the observations in Figure 5A-C. This evidence confirms that the recovery process involves an initial transition of the hcp lattice to an intermediate lattice

before returning to the bcc lattice during unloading. This process occurs throughout the phase boundary, resulting in the migration of the phase boundary and ultimately the full recovery of the bcc phase.

We also performed the MD simulations for other four NWs with the longitudinal direction of [11$\bar{2}$], [001], and [111], respectively [Supplementary Figures 6-9]. For the [11$\bar{2}$] and [001] oriented NWs, their plastic deformation is governed by both bcc-hcp and bcc-fcc phase transitions [Supplementary Figures 6-8]. For the [111]-oriented NW, only bcc-hcp phase transition occurs, while this phase transition cannot continue to occur uniformly in subsequent deformation and leads to early necking [Supplementary Figure 9]. Moreover, we notice that the NW can re-orient from <001> orientation to <110> during the deformation process [Supplementary Figure 8E and F], leading its subsequent deformation to be governed mainly by the bcc-hcp phase transition. This usual deformation results in the NW exhibiting a large homogeneous deformation capacity. In addition, we performed the MD simulations for another three [1$\bar{1}$0]-oriented NWs with rectangular, rhombic and round cross-sections, respectively. The results show that the bcc-hcp phase transition is also the dominant deformation mode [Supplementary Figures 10-12]. These indicate that bcc-hcp phase transition prefers to occur in those NWs with <110> orientation and surface effect on the bcc-hcp phase transition is not obvious. In order to reveal why the bcc-hcp phase transition is more preferred for the <110>-orientation NWs, the orientation relationship of the bcc/hcp and the bcc-hcp phase transition path is illustrated in Supplementary Figure 13. The crystallographic relationship between the bcc structure and the hcp structure before and after the phase transition is $\{110\}_{bcc}||\{0002\}_{hcp}$. It shows that the bcc lattice transforms into the hcp lattice via tension along the [1$\bar{1}$0] direction and compression along the [001] direction[40]. Therefore, tensile loading along the <110> direction is more likely to initiate the bcc-hcp phase transition.

Furthermore, we also conducted MD simulations on NWs with sizes of 24.1 nm × 6.3 nm × 6 nm and 48.4 nm × 16.7 nm × 16.3 nm [see Supplementary Figures 14 and 15]; the results show that their deformation is also governed by bcc-hcp phase transition. This phase transition is the predominant deformation mode, even in relatively large-sized NWs. Meanwhile, it should be noted that our simulations are based on NWs with only several tens of nanometers. As for the relatively large size and bulk HEAs, the defects (e.g., dislocations, grain boundaries) and more complex stress condition effect on this reversible phase transition cannot be ignored. We therefore suppose that the occurrence of large-scale continuous reversible phase transition in relatively large-sized sample and bulk HEA is difficult. Such reversible phase transition may occur locally in bulk HEAs at relatively high temperatures due to thermal fluctuations[17]. Moreover, due to the computational capability limitation, MD simulation-operational models are generally small (only a few tens of nanometers). MD simulations demonstrate a notable degree of efficacy in the context of nanoscale samples. When the samples are micrometer-scale or even larger, the deformation mode may change. It should be cautious when using MD to investigate the deformation mechanism of those relatively large-sized and bulk HEAs.

Additionally, it should be noted that there are a considerable number of local structures and local atomic clusters in HEAs[31-34], which may significantly affect the deformation mechanisms of HEAs. Thus, we also constructed other two typical NWs with different SRO degrees by hybrid MC/MD simulations. Their SRO degrees are described by WCPs [see Supplementary Figure 16]. The deformation mechanism of these two NWs under tensile loading is shown in Supplementary Figures 17 and 18. It was found that these two NWs also accommodate plastic deformation through the bcc-hcp phase transition. These are similar to the results shown in Figure 2. Meanwhile, it should be noted that the homogeneous strain decreases as the SRO degree increases, indicating that the SRO degree can significantly affect the further propagation of the hcp phase

[see Supplementary Figures 17 and 18]. In addition, we also investigated the reverse phase transition process of these two typical NWs, as shown in Supplementary Figures 19 and 20; the reverse bcc-hcp transition occurs not only at the bcc-hcp phase boundary but can also be initiated in the hcp region. This suggests that the local SRO can provide additional sites for the initiation of the reverse bcc-hcp transition. Thus, the SRO has a slight effect on the reversibility of the phase transition. We have calculated the energy barriers of the bcc-hcp transition and its reverse process using the nudged elastic band method. The energy-barrier curves show that both the bcc-hcp transition [Supplementary Figure 21] and its reverse process [Supplementary Figure 22] have non-singular energy barriers. This is because the inhomogeneously distributed elements lead to local variations in the energy barriers for the phase transition. Thus, the SRO can affect the local deformation mechanism and the phase transition. This explains why the bcc-hcp transition [Supplementary Figures 17 and 18] and its reverse [Supplementary Figures 19 and 20] process are slightly different for those NWs with different SRO. A previous study[17] also proposed that SRO local structures rich with elements Hf, Ti and Zr can lower the nucleation barrier for bcc-hcp transition. These indicate that the local structures can affect the energy barriers of phase transition and mechanical behaviors of HEAs, and they are expected to be modified via alloying and processing conditions.

According to previous theoretical models, simulations, and experiments, the deformation of fcc structured HEAs is always controlled by twinning and dislocation activities[12]. For large-size bcc structured HEAs, most previous research has suggested that their deformation is primarily controlled by screw dislocations with a Burgers vector of 1/2 <111>[13-16,20,26,41]. Lee *et al.* proposed that edge dislocation activities enable bcc structured HEAs to exhibit high strength at elevated temperatures[16]. Regarding the bcc-hcp phase transition, previous studies suggested that it rarely occurs during room temperature deformation. Huang *et al.* reported that this phase transition can occur at high temperatures in bcc structured HEAs[17]. In contrast, our simulation reveals that the deformation of HfNbTaTiZr HEA NWs is governed by the bcc-hcp phase transition at room temperature, which differs from prior research on bcc structured HEAs. More importantly, it is widely believed that plastic deformation usually leads to permanent structural changes in large-size single-crystal or coarse-grained polycrystalline metals, which are generally irreversible. Our current study finds that the plastic deformation of nano-sized $[1\bar{1}0]$-oriented HfNbTaTiZr HEA NWs is governed by a single homogeneous bcc-hcp phase transition, and that this bcc-hcp phase transition is reversible. Although reversible phase transitions have been reported in shape memory alloys[27,28], and reversible deformation twinning under heating has been predicted in ~2 nm-sized pure FCC metals[42,43], reports of the bcc-hcp phase transition and its reversibility in nanoscale bcc structured HEAs are rare. Since microstructural evolution can significantly influence the mechanical properties of materials, this discovery offers valuable insights for designing HEAs with optimized properties.

CONCLUSIONS

In conclusion, the mechanical behavior of HfNbTaTiZr HEA NWs at room temperature was investigated using MD simulations. It was found that the plastic deformation of HfNbTaTiZr NWs under tension was governed by bcc-hcp phase transition. This bcc-hcp phase transition occurred via Bain strain, which involves the distortion and rearrangement of lattice spacing and bond angles, ultimately leading to the formation of the hcp phase. Remarkably, this phase transition was reversible upon unloading. Our results offer a comprehensive understanding of the deformation mechanism of nano-sized HEAs at room temperature and provide valuable insights for the design and application of such materials.

DECLARATIONS

Authors' contributions

Conceptualization: Wang, L.; Han, X.

Formal analysis and software: Wang, Z.; Li, S.; Lian, H.; Zhao, Y.; Li, Z.
Data curation and writing-original draft: Wang, Z.; Li, S.; Wang, L.
Funding acquisition, supervision, validation and writing-review & editing: Long, H.; Wang, L.; Zhai, Y.; Wang, Z.

Availability of data and materials

Some results supporting the study are presented in the Supplementary Materials. Other raw data that support the findings of this study are available from the corresponding author upon reasonable request.

Financial support and sponsorship

This work was supported by the National Key R & D Program of China (2021YFA1200201), the Natural Science Foundation of China (12174014), Beijing Outstanding Young Scientists Projects (BJJWZYJH01201910005018) and Young Elite Scientists Sponsorship Program by CAST for Doctoral Student.

Conflicts of interest

Han, X. is an Editorial Board Member of the journal *Microstructures*. Han, X. was not involved in any steps of editorial processing, notably including reviewer selection, manuscript handling, or decision-making, while the other authors have declared that they have no conflicts of interest.

Ethical approval and consent to participate

Not applicable.

Consent for publication

Not applicable.

REFERENCES

1. Chen, T. K.; Shun, T. T.; Yeh, J. W.; Wong, M. S. Nanostructured nitride films of multi-element high-entropy alloys by reactive DC sputtering. *Surf. Coat. Technol.* **2004**, *188-9*, 193-200. DOI
2. Chen, M. R.; Lin, S. J.; Yeh, J. W.; Chuang, M. H.; Chen, S. K.; Huang, Y. S. Effect of vanadium addition on the microstructure, hardness, and wear resistance of $Al_{0.5}$CoCrCuFeNi high-entropy alloy. *Metall. Mater. Trans. A.* **2006**, *37*, 1363-9. DOI
3. Tung, C. C.; Yeh, J. W.; Shun, T. T.; Chen, S. K.; Huang, Y. S.; Chen, H. C. On the elemental effect of AlCoCrCuFeNi high-entropy alloy system. *Mater. Lett.* **2007**, *61*, 1-5. DOI
4. Senkov, O. N.; Wilks, G. B.; Miracle, D. B.; Chuang, C. P.; Liaw, P. K. Refractory high-entropy alloys. *Intermetallics* **2010**, *18*, 1758-65. DOI
5. Liu, C. M.; Wang, H. M.; Zhang, S. Q.; Tang, H. B.; Zhang, A. L. Microstructure and oxidation behavior of new refractory high entropy alloys. *J. Alloys. Compd.* **2014**, *583*, 162-9. DOI
6. George, E. P.; Raabe, D.; Ritchie, R. O. High-entropy alloys. *Nat. Rev. Mater.* **2019**, *4*, 515-34. DOI
7. Li, Z.; Zhao, S.; Ritchie, R. O.; Meyers, M. A. Mechanical properties of high-entropy alloys with emphasis on face-centered cubic alloys. *Prog. Mater. Sci.* **2019**, *102*, 296-345. DOI
8. George, E. P.; Curtin, W. A.; Tasan, C. C. High entropy alloys: a focused review of mechanical properties and deformation mechanisms. *Acta. Mater.* **2020**, *188*, 435-74. DOI
9. Otto, F.; Dlouhý, A.; Somsen, C.; Bei, H.; Eggeler, G.; George, E. P. The influences of temperature and microstructure on the tensile properties of a CoCrFeMnNi high-entropy alloy. *Acta. Mater.* **2013**, *61*, 5743-55. DOI
10. He, J. Y.; Zhu, C.; Zhou, D. Q.; Liu, W. H.; Nieh, T. G.; Lu, Z. P. Steady state flow of the FeCoNiCrMn high entropy alloy at elevated temperatures. *Intermetallics* **2014**, *55*, 9-14. DOI
11. Li, Y. X.; Nutor, R. K.; Zhao, Q. K.; et al. Unraveling the deformation behavior of the $Fe_{45}Co_{25}Ni_{10}V_{20}$ high entropy alloy. *Int. J. Plast.* **2023**, *165*, 103619. DOI
12. Zhang, Q.; Huang, R.; Jiang, J.; et al. Size effects and plastic deformation mechanisms in single-crystalline CoCrFeNi micro/

nanopillars. *J. Mech. Phys. Solids.* **2022**, *162*, 104853. DOI
13. Li, C.; Li, J. C.; Zhao, M.; Jiang, Q. Effect of alloying elements on microstructure and properties of multiprincipal elements high-entropy alloys. *J. Alloys. Compd.* **2009**, *475*, 752-7. DOI
14. Ye, Y. F.; Liu, C. T.; Yang, Y. A geometric model for intrinsic residual strain and phase stability in high entropy alloys. *Acta. Mater.* **2015**, *94*, 152-61. DOI
15. Couzinié, J. P.; Lilensten, L.; Champion, Y.; Dirras, G.; Perrière, L.; Guillot, I. On the room temperature deformation mechanisms of a TiZrHfNbTa refractory high-entropy alloy. *Mater. Sci. Eng. A.* **2015**, *645*, 255-63. DOI
16. Lee, C.; Maresca, F.; Feng, R.; et al. Strength can be controlled by edge dislocations in refractory high-entropy alloys. *Nat. Commun.* **2021**, *12*, 5474. DOI PubMed PMC
17. Huang, X.; Liu, L.; Liao, W.; Huang, J.; Sun, H.; Yu, C. Characterization of nucleation behavior in temperature-induced BCC-to-HCP phase transformation for high entropy alloy. *Acta. Metall. Sin.* **2021**, *34*, 1546-56. DOI
18. Wu, Y. D.; Cai, Y. H.; Wang, T.; et al. A refractory $Hf_{25}Nb_{25}Ti_{25}Zr_{25}$ high-entropy alloy with excellent structural stability and tensile properties. *Mater. Lett.* **2014**, *130*, 277-80. DOI
19. Senkov, O. N.; Scott, J. M.; Senkova, S. V.; Miracle, D. B.; Woodward, C. F. Microstructure and room temperature properties of a high-entropy TaNbHfZrTi alloy. *J. Alloys. Compd.* **2011**, *509*, 6043-8. DOI
20. Mills, L. H.; Emigh, M. G.; Frey, C. H.; et al. Temperature-dependent tensile behavior of the HfNbTaTiZr multi-principal element alloy. *Acta. Mater.* **2023**, *245*, 118618. DOI
21. Jeon, S.; Heo, T.; Hwang, S. Y.; et al. Reversible disorder-order transitions in atomic crystal nucleation. *Science* **2021**, *371*, 498-503. DOI
22. Fang, Q.; Chen, Y.; Li, J.; et al. Probing the phase transformation and dislocation evolution in dual-phase high-entropy alloys. *Int. J. Plast.* **2019**, *114*, 161-73. DOI
23. Jafary-zadeh, M.; Aitken, Z. H.; Tavakoli, R.; Zhang, Y. On the controllability of phase formation in rapid solidification of high entropy alloys. *J. Alloys. Compd.* **2018**, *748*, 679-86. DOI
24. Santodonato, L. J.; Liaw, P. K.; Unocic, R. R.; Bei, H.; Morris, J. R. Predictive multiphase evolution in Al-containing high-entropy alloys. *Nat. Commun.* **2018**, *9*, 4520. DOI PubMed PMC
25. Kostiuchenko, T.; Körmann, F.; Neugebauer, J.; Shapeev, A. Impact of lattice relaxations on phase transitions in a high-entropy alloy studied by machine-learning potentials. *NPJ. Comput. Mater.* **2019**, *5*, 195. DOI
26. Li, S.; Ding, X.; Li, J.; Ren, X.; Sun, J.; Ma, E. High-efficiency mechanical energy storage and retrieval using interfaces in nanowires. *Nano. Lett.* **2010**, *10*, 1774-9. DOI
27. Wen, Y. H.; Peng, H. B.; Raabe, D.; Gutierrez-Urrutia, I.; Chen, J.; Du, Y. Y. Large recovery strain in Fe-Mn-Si-based shape memory steels obtained by engineering annealing twin boundaries. *Nat. Commun.* **2014**, *5*, 4964. DOI PubMed
28. Sun, J. W.; Wang, S. L.; Yan, Z. W.; Peng, H. B.; Wen, Y. H. Origin of shape memory effect in Co-Ni alloys undergoing fcc⇌hcp martensitic transformation. *Mater. Sci. Eng. A.* **2015**, *639*, 456-64. DOI
29. Plimpton, S. Fast parallel algorithms for short-range molecular dynamics. *J. Comput. Phys.* **1995**, *117*, 1-19. DOI
30. Lee, B.; Baskes, M.; Kim, H.; Koo, C. Y. Second nearest-neighbor modified embedded atom method potentials for bcc transition metals. *Phys. Rev. B.* **2001**, *64*, 184102. DOI
31. Cowley, J. M. An approximate theory of order in alloys. *Phys. Rev.* **1950**, *77*, 669-75. DOI
32. de Fontaine, D. The number of independent pair-correlation functions in multicomponent systems. *J. Appl. Cryst.* **1971**, *4*, 15-9. DOI
33. Ceguerra, A. V.; Powles, R. C.; Moody, M. P.; Ringer, S. P. Quantitative description of atomic architecture in solid solutions: a generalized theory for multicomponent short-range order. *Phys. Rev. B.* **2010**, *82*, 132201. DOI
34. Cantor, B. Local nanostructure in multicomponent high-entropy materials. *High. Entropy. Alloy. Mater.* **2024**, *2*, 277-306. DOI
35. Cowley, J. M. X-ray measurement of order in single crystals of Cu_3Au. *J. Appl. Phys.* **1950**, *21*, 24-30. DOI
36. Chen, S.; Aitken, Z. H.; Pattamatta, S.; et al. Simultaneously enhancing the ultimate strength and ductility of high-entropy alloys via short-range ordering. *Nat. Commun.* **2021**, *12*, 4953. DOI PubMed PMC
37. Larsen, P. M. Revisiting the common neighbour analysis and the centrosymmetry parameter. *ArXiv* **2003**, *2020*, 08879. DOI
38. Stukowski, A. Visualization and analysis of atomistic simulation data with OVITO-the open visualization tool. *Model. Simul. Mat. Sci. Eng.* **2010**, *18*, 015012. DOI
39. Alippi, P.; Marcus, P. M.; Scheffler, M. Strained tetragonal states and bain paths in metals. *Phys. Rev. Lett.* **1997**, *78*, 3892-5. DOI
40. Obasi, G. C.; Birosca, S.; Quinta da Fonseca, J.; Preuss, M. Effect of β grain growth on variant selection and texture memory effect during α→β→α phase transformation in Ti-6 Al-4 V. *Acta. Mater.* **2012**, *60*, 1048-58. DOI
41. Yasuda, H. Y.; Yamada, Y.; Cho, K.; Nagase, T. Deformation behavior of HfNbTaTiZr high entropy alloy singe crystals and polycrystals. *Mater. Sci. Eng. A.* **2021**, *809*, 140983. DOI
42. Liang, W.; Zhou, M.; Ke, F. Shape memory effect in Cu nanowires. *Nano. Lett.* **2005**, *5*, 2039-43. DOI PubMed
43. Park, H. S.; Gall, K.; Zimmerman, J. A. Shape memory and pseudoelasticity in metal nanowires. *Phys. Rev. Lett.* **2005**, *95*, 255504. DOI PubMed